



Article

# Preparation and Performance of Carbon-Based Ce-Mn Catalysts for Efficient Degradation of Acetone at Low Temperatures

Tong Li <sup>1,2</sup>, Zhibo Wang <sup>1,3</sup>, Yue Shi <sup>1,3</sup> and Xiaolong Yao <sup>1,3,\*</sup>

<sup>1</sup> School of Ecology and Environment, Beijing Technology and Business University, Beijing 100048, China

<sup>2</sup> SINOPEC (Beijing) Research Institute of Chemical Industry Co., Ltd., Beijing 100013, China

<sup>3</sup> State Environmental Protection Key Laboratory of Food Chain Pollution Control, Beijing Technology and Business University, Beijing 100048, China

\* Correspondence: yaoxiaolong@btbu.edu.cn; Tel.: +86-10-6898-4448

**Abstract:** Based on the porous carbon material from citric acid residue, catalysts of different Ce-Mn ratios were prepared with incipient-wetness impregnation (IWI) to delve into their acetone-degrading performance and relevant mechanisms. When the Ce-Mn molar ratio is 0.8, the prepared catalyst Ce<sub>0.8</sub>-Mn/AC shows abundant and uniformly dispersed Mn and Ce particles on the surface. The content of Mn and Ce on the Ce<sub>0.8</sub>-Mn/AC surface reaches 5.64% and 0.75%, respectively. At the acetone concentration of 238 mg/m<sup>3</sup> (100 ppm), the laws of acetone degradation in different catalysts at different catalyzing temperatures and with various oxygen concentrations were studied, and we found that the rate of acetone degradation by Ce<sub>0.8</sub>-Mn/AC can exceed 90% at 250 °C. Cerium oxide and manganese oxide are synergistic in the catalytic degradation of acetone. Adding cerium to manganese-based catalysts can increase the oxygen migration rate in the catalysts and thus raise the reduction rate of lattice oxygen in manganese oxide. The results offer new ideas and approaches for the efficient and comprehensive utilization of bio-fermentation by-products, and for the development of cheap and high degradation performance catalysts for acetone.

**Keywords:** acetone; Ce<sub>0.8</sub>-Mn/AC; efficient degradation; low temperatures



**Citation:** Li, T.; Wang, Z.; Shi, Y.; Yao, X. Preparation and Performance of Carbon-Based Ce-Mn Catalysts for Efficient Degradation of Acetone at Low Temperatures. *Int. J. Environ. Res. Public Health* **2022**, *19*, 16879. <https://doi.org/10.3390/ijerph192416879>

Academic Editor: William A. Toscano

Received: 17 November 2022

Accepted: 9 December 2022

Published: 15 December 2022

**Publisher's Note:** MDPI stays neutral with regard to jurisdictional claims in published maps and institutional affiliations.



**Copyright:** © 2022 by the authors. Licensee MDPI, Basel, Switzerland. This article is an open access article distributed under the terms and conditions of the Creative Commons Attribution (CC BY) license (<https://creativecommons.org/licenses/by/4.0/>).

## 1. Introduction

China is the world's largest producer and exporter of citric acid, whose yield accounts for about 53% of the world's total production [1]. In citric acid processing, bio-fermentation is the primary production process. The process produces both citric acid intermediates and many volatile organic by-products, among which acetone is one of the most considerable amounts [2,3]. Acetone can involve photochemical reactions [4,5], and can be oxidated to organic acids (such as formic acid and acetic acid) to promote the formation of secondary organic aerosols (SOA) [6,7]. Meanwhile, acetone is chronically toxic to human body, and can lead to chronic neurotoxicity and impair renal and liver functions [8,9]. Therefore, seeking the appropriate purification technology for acetone from citric acid production has become a significant issue in this research field.

Catalytic oxidation is one of standard methods to purify VOCs (volatile organic compounds), especially for the VOCs with low concentrations and no recycling value [10,11]. Catalytic performance of catalysts depends on the properties of active components in the catalyst. According to relevant degradation mechanisms of Mars–van Krevelen (MVK) [12,13], Langmuir–Hinshelwood (L-H) [13,14], and Eley–Ridea (E-R) [15], particles of the active components coat the supporting carrier surface in the preparation process. In the process of degradation, acetone molecules are converted into inorganic compounds through the interaction with lattice oxygen and adsorption oxygen on the surface of the catalyst carrier [16]. In the meantime, after the metal oxide releases lattice oxygen, oxygen vacancies will be formed on the catalyst surface [17]. These reduction centers are regenerated through

the compensation of oxygen or oxygen atoms in the carrier gas. Therefore, the type and dispersibility of active components on the carrier surface and their ability to transfer electrons are the main influencing factors of acetone degradation [18].

Some researches indicated that the reduction catalysts carrying precious metals (gold, platinum, etc.) show good acetone-catalyzing performance and support acetone degradation at low temperatures [19–21]. However, they are usually expensive to prepare and prone to poisoning [22]. Therefore, catalysts carrying cheaper metallic oxides (ZnO, Mn<sub>2</sub>O<sub>3</sub>, CeO<sub>2</sub>, etc.) are more competitive in the purification of industrial waste gas [23–26]. Studies indicate that Cu can improve its oxygen storage capacity by reducing the activation energy of Ce<sup>4+</sup> reduction during the catalytic oxidation of acetone with Cu<sub>0.13</sub>Ce<sub>0.87</sub>O<sub>y</sub> [27]. The perovskite-type La<sub>0.6</sub>Pb<sub>0.2</sub>Ca<sub>0.2</sub>MnO<sub>3</sub> catalyst has a large amount of manganese ions with different valences and can provide many oxygen vacancies to degrade over 95% acetone at 300 °C [28]. These results indicate that using Ce and Mn oxides as active components is possible to effectively degrade acetone.

On the other hand, appropriate catalyst carriers are of great significance to improving the dispersibility of active components. Common catalyst carriers include mesoporous aluminum silicates, graphene, zeolite molecular sieves (ZMS), biomass-activated carbon, and natural minerals [29–32]. Carbon-based carriers have attracted much attention because of their advantages of developed pore structures, large specific surface area, and low price in recent years [33–35]. To prepare carbon-based carriers with a developed pore structure and good dispersibility of active components have become new research focuses [36,37]. In the preliminary study, we used citric acid residue to prepare the porous carbon material. Its specific surface area exceeds 1000 m<sup>2</sup>/g, and it has suitable mesoporous and microporous structures [3]. These results indicate that it is possible to prepare carbon-based catalysts with good dispersibility of active components.

Here, we prepared catalysts of different Ce-Mn ratios through the IWV with the porous carbon material prepared from citric acid residue as the carrier. Their physical and chemical properties were characterized, and their degrading performances for acetone were studied with a catalyst testing device, and the corresponding degradation mechanisms are discussed as well. The research results offer new ideas and approaches for the efficient and comprehensive utilization of by-products in the bio-fermentation industry and for the development of cheap and high degradation performance catalysts for acetone at low temperatures.

## 2. Materials and Methods

### 2.1. Materials

Phosphoric acid (85%) and manganese sulphate (analytical grade) were obtained from Sinopharm Group (Beijing, China). Cerium nitrate (analytical grade) was purchased from Aladdin Reagent Co., Ltd. (Shanghai, China). Citric acid residue (CAR) waste was collected from a citric acid plant in Shandong Province, China. High-purity standard gases of acetone and nitrogen were obtained from Zhaoge Gas Technology Co., Ltd. (Beijing, China). All solutions were prepared with ultrapure water produced by Milli-Q Academic (Boston, MA, USA).

### 2.2. Catalysts Preparation

The activated carbon (AC) carrier was prepared with citric acid residue waste following the method reported in a previous study [3]. The Ce-Mn mixed impregnation solutions were prepared with the solutions of cerium nitrate and manganese sulfate. The mass fraction of Mn in the mixed solution was maintained at 2.0 wt%, and the mass fraction of Ce in the mixed solution was changed at the molar ratios of Ce/Mn 0.0, 0.2, 0.4, 0.6, 0.8, and 1.0.

To prepare catalysts, 10 g AC carrier was first immersed in 100 mL of the Ce-Mn mixed impregnation solution, and ultrasonic treatment lasted for 1 h at room temperature. Then, the samples were dried in a vacuum drying oven at 60 °C for 4 h to remove residue water.

After that, the dried sample was heated to 400 °C at a speed of 10 °C/min and maintained for 3 h in a tube furnace. Finally, the samples were cooled to room temperature and sealed at low temperatures. The samples were labelled as Ce<sub>x</sub>-Mn/AC (x indicates the molar ratio of Ce to Mn).

### 2.3. Catalysts Characterization

The N<sub>2</sub> adsorption–desorption isotherms and the pore size distribution of Ce<sub>x</sub>-Mn/AC were characterized by an automated gas sorption analyzer (Quantachrome, Nova 2000e, Boynton Beach, FL, USA). Powder XRD patterns of the samples were recorded on an XRD diffractometer (Bruker, D8 ADVANCE, Ettlingen, Germany). The data were recorded at a scan rate of 10°/min, and the diffraction peak of the crystalline phase was measured in a scanning range of 2θ = 10–80° and then compared with the diffraction peak of the standard compound reported in the JCPDS data file. The sample surfaces were analyzed using X-ray photoelectron spectroscopy (XPS) (Thermo Fisher Scientific Inc., Waltham, MA, USA). All binding energies of Ce<sub>3d</sub>, Mn<sub>2p</sub>, and O<sub>1s</sub> were referenced to the neutral C<sub>1s</sub> peak at 284.6 eV to compensate for surface charging effects. XPS peak 4.1 software (version number: 4.01) was used to fit the XPS spectra peaks, and the full width at half maximum (FWHM) was maintained constant for all components in a particular spectrum. A scanning electron microscope (SEM) (Merlin compact, Zeiss, Oberkochen, Germany) and a transmission electron microscope (TEM) (FEI, Philips Tecnai F20, Hillsboro, OR, USA) were used to study the dispersity of active components on the catalyst sample surfaces.

### 2.4. Catalytic Experiments

Acetone catalytic degradation experiments were carried out in a fixed-bed catalytic setup, and the experimental apparatus is shown in Figure 1. The prepared high-purity standard gases of acetone were placed in gas cylinders. When the experiment started, the gas channel was opened by a valve, and the mass flow controllers adjusted the flow rate of the stream at 100 mL/min. The gas stream was preheated to 80 °C before entering the catalytic bed. Then, 0.5 g of outgassed catalyst was loaded into a catalytic bed (φ 6 mm × 150 mm). A filter plate was located at the bottom of the column as a support of the catalytic bed. The inlet concentration of acetone (C<sub>in</sub>) was maintained at 238 mg/m<sup>3</sup> (100 ppm) during the degradation experiments, and the acetone vapor flowed through the fixed bed from the bottom of the catalytic bed. The catalytic reaction temperature was controlled at 25, 80, 120, 170, 220, 250, and 280 °C. The temperature was kept constant for 30 min at each temperature test point in order to determine the degradation conversion of catalysts for acetone. In addition, the optimum catalyst for acetone conversion was selected to study the degradation of acetone under different catalytic reaction temperatures and different oxygen contents in waste gas.

The inlet concentrations (C<sub>in</sub>, mg/m<sup>3</sup>) and outlet concentrations (C<sub>out</sub>, mg/m<sup>3</sup>) of acetone were measured by a gas chromatography instrument (Techcomp GC7900, China) equipped with a TM-624 quartz capillary column (length × inner diameter × thickness, 60 m × 0.32 mm × 2.0 μm) and a flame-ionization detector. Operating conditions were as follows: oven temperature, 65 °C; detector temperature, 220 °C; carrier gas, N<sub>2</sub> at 20 mL/min. The acetone conversion (ω, %) was calculated as follows [38,39]:

$$\omega = (1 - C_{in}/C_{out}) \times 100\% \quad (1)$$

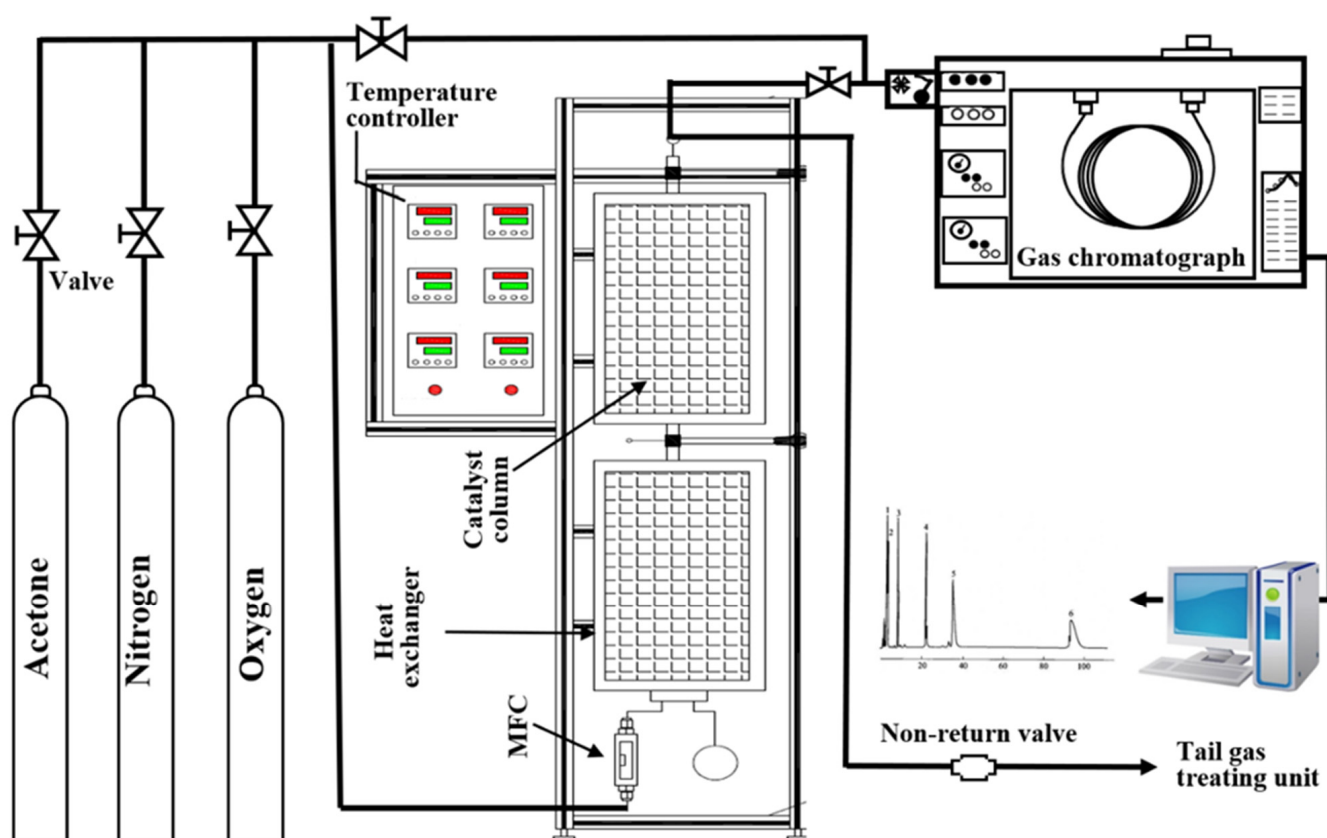


Figure 1. Configuration of the experimental apparatus.

### 3. Results and Discussion

#### 3.1. Catalyst Characterization

Figure 2a shows the  $N_2$  adsorption–desorption isotherms of the AC carrier and prepared catalysts. According to the ICPUC classification of adsorption isotherms, the  $N_2$  adsorption–desorption isotherms of the AC carrier and the prepared carbon-based catalysts are IV-type adsorption isotherms [40]. The hysteresis loops present in the adsorption–desorption isotherm curves between the partial pressures of 0.4 and 1.0 because of the mesoporous structures in the catalysts [41]. Figure 2b shows the pore size distribution of the AC carrier and catalysts. The pore sizes are mostly at 1.2, 1.5, 1.8, 2.3, or 3.8 nm for the AC carrier. After carrying active components, the pore volume of the catalysts is more minor than the original AC carrier because of the deposition of active components onto the AC surfaces [42–44]. Table 1 shows the specific surface areas and pore volumes of the prepared catalyst materials. The AC carrier features a large specific surface area and a rich microporous structure. The specific surface area and pore volume of the AC reach  $1400.2 \text{ m}^2/\text{g}$  and  $0.793 \text{ cm}^3/\text{g}$ , respectively. The specific surface areas and pore volumes of all catalysts were reduced after carrying active components. Among them,  $\text{Ce}_{0.8}\text{-Mn}/\text{AC}$  showed maximizing reduction in the specific surface area and pore volume, dropping to  $645.18 \text{ m}^2/\text{g}$  and  $0.358 \text{ cm}^3/\text{g}$ , respectively. The results indicate that the active components were successfully loaded on the carriers. Moreover, an appropriate Ce/Mn molar ratio better helps to load the active components onto the carriers [45,46].

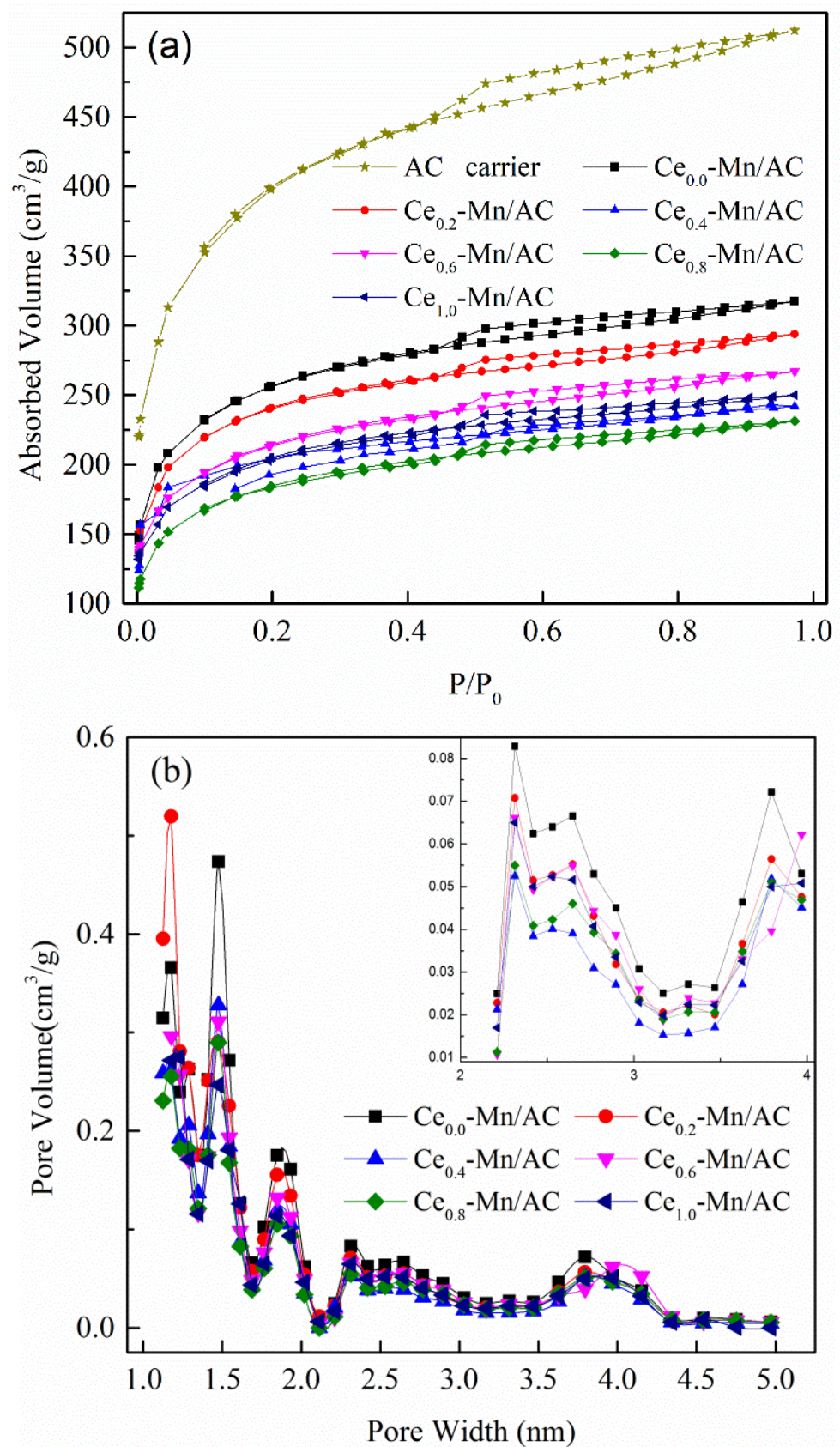
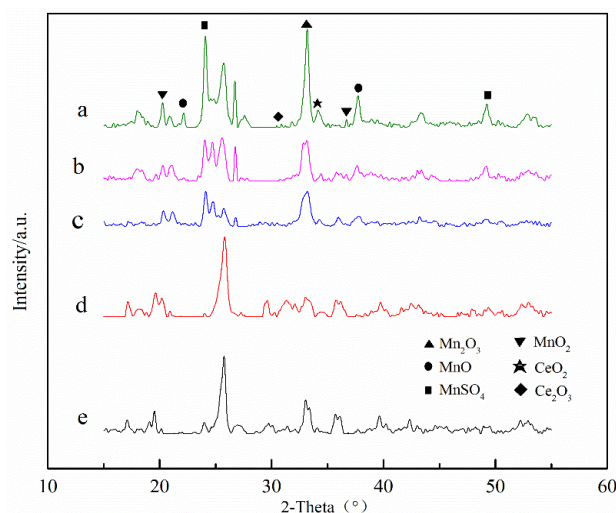


Figure 2. N<sub>2</sub> adsorption–desorption isotherms (a) and DFT pore size distributions (b) for samples.

**Table 1.** Porous structural parameters of samples.

Catalyst	S <sub>BET</sub> (m <sup>2</sup> /g)	Mesoporous Volume (cm <sup>3</sup> /g)	Total Pore Volume (cm <sup>3</sup> /g)
Biomass-activated carbon	1400.25	0.179	0.793
Ce <sub>0.0</sub> -Mn/AC	918.07	0.096	0.491
Ce <sub>0.2</sub> -Mn/AC	837.83	0.084	0.454
Ce <sub>0.4</sub> -Mn/AC	702.42	0.071	0.376
Ce <sub>0.6</sub> -Mn/AC	776.49	0.084	0.413
Ce <sub>0.8</sub> -Mn/AC	645.18	0.074	0.358
Ce <sub>1.0</sub> -Mn/AC	725.98	0.113	0.387

X-ray diffraction (XRD) results of the catalysts are shown in Figure 3. Catalysts of different Ce-Mn ratios were relatively consistent in diffraction peak position and peak pattern. All samples showed sharp characteristic diffraction peaks at  $2\theta = 24.0^\circ$  and  $49.1^\circ$ , whose position corresponds to the standard card JCPDS PDF#73-1361, indicating the presence of MnSO<sub>4</sub> in the samples. All samples showed characteristic diffraction peaks at  $2\theta = 21.7^\circ$  and  $37.9^\circ$ , indicating the presence of MnO in the samples (JCPDS 12-0141). In addition, the map of diffraction peaks shows characteristic peaks of Mn<sub>2</sub>O<sub>3</sub> and MnO<sub>2</sub> (JCPDS 41.1442, JCPDS 42-1169). These results indicate that manganese was successfully loaded onto the carriers, and part of the MnSO<sub>4</sub> was converted into MnO<sub>x</sub> (including Mn<sub>2</sub>O<sub>3</sub> and MnO<sub>2</sub>) during the firing process. Additionally, after Ce doping, the absorption peaks of CeO<sub>2</sub> and Ce<sub>2</sub>O<sub>3</sub> (PDF 34-0394, PDF 44-1086) presented in the diffraction peaks of the catalyst samples [40,47], indicating the conversion of ceric nitrate into CeO<sub>2</sub> and Ce<sub>2</sub>O<sub>3</sub>. The signal of the MnO<sub>x</sub> absorption peaks was weakened, indicating that Ce doping can improve MnO<sub>x</sub> dispersibility in the carriers [47–49].



**Figure 3.** XRD experimental results of different catalysts. (a) Ce<sub>0.0</sub>-Mn/AC; (b) Ce<sub>0.2</sub>-Mn/AC; (c) Ce<sub>0.4</sub>-Mn/AC; (d) Ce<sub>0.8</sub>-Mn/AC; (e) Ce<sub>1.0</sub>-Mn/AC.

Figure 4 presents the XPS maps of Mn<sub>2p</sub>, Ce<sub>3d</sub>, and O<sub>1s</sub> in the Ce<sub>0.0</sub>-Mn/AC, Ce<sub>0.4</sub>-Mn/AC, and Ce<sub>0.8</sub>-Mn/AC samples. For the XPS maps of Mn<sub>2p</sub> (Figure 4a), the fitted peaks with binding energies of 639.0, 641.3, and 642.4 eV correspond to Mn<sup>2+</sup>, Mn<sup>3+</sup>, and Mn<sup>4+</sup>, respectively [26,50]. The content of oxidizing Mn<sup>4+</sup> and Mn<sup>3+</sup> in different samples was calculated by peak fitting software. As the proportion of Ce increased in the sample preparation process, Mn<sup>4+</sup>/Mn<sup>3+</sup> increased from 0.69 to 3.02, and the content of Mn<sup>4+</sup> with higher oxidizing performance also increased gradually. A higher proportion of Mn<sup>4+</sup> is more conducive to the oxidation of organic matter [51]. For the XPS maps of Ce<sub>3d</sub> (Figure 4b), the Ce<sub>3d</sub> spectrum can be broken down to eight peaks according to relevant literature [25,36,52–55], including four pairs of spin-splitting primes of Ce<sub>3d</sub> that are marked

as  $v$  and  $u$ . Among them,  $v$ ,  $v_1$ ,  $v_2$ , and  $v_3$  are the spin orbits of  $Ce_{3d}5/2$ , and  $u$ ,  $u_1$ ,  $u_2$ , and  $u_3$  are the spin orbits of  $Ce_{3d}3/2$ . The  $(u_1 + v_1)$  binding energy peak is attributed to the  $3d^{10}4f^1$  electronic state of  $Ce^{3+}$ , and the  $(u + u_2 + u_3 + v + v_2 + v_3)$  binding energy peak is attributed to the  $3d^{10}4f^0$  electronic state of  $Ce^{4+}$ . The  $Ce^{3+}$  content represents the number of oxygen vacancies on the catalyst surface; the higher content of  $Ce^{3+}$ , the more oxygen vacancies there are [37,56,57].  $Ce^{3+}$  and  $Ce^{4+}$  were found on the surface of both  $Ce_{0.4}\text{-Mn/AC}$  and  $Ce_{0.8}\text{-Mn/AC}$ , and the ratio of  $Ce^{4+}/Ce^{3+}$  was 2.38 and 1.08, respectively. In addition,  $Ce^{3+}$  on  $Ce_{0.8}\text{-Mn/AC}$  was higher than that on  $Ce_{0.4}\text{-Mn/AC}$  [48]. Therefore, higher cerium content is conducive to the formation of more oxygen vacancies on the catalyst surface, and better helps to increase the oxygen transfer rate in the later catalytic degradation of acetone [51,58]. For the XPS maps of  $O_{1s}$  (Figure 4c), the fitted peaks with a binding energy of 531.8 and 533.7 eV correspond to lattice oxygen ( $O_\alpha$ ) and adsorption oxygen ( $O_\beta$ ), respectively [47,53,59]. As the Ce increased, the numbers of both adsorption oxygen and lattice oxygen on the catalyst surface, as well as the proportion of lattice oxygen, increased. The  $O_\alpha/O_\beta$  ratio on the  $Ce_{0.8}\text{-Mn/AC}$  surface reached 10.08. This is partly due to the fact that a higher content of  $Mn^{4+}$  is more attractive lattice oxygen, and a higher content of  $Ce^{3+}$  is more likely to form oxygen vacancies [60].

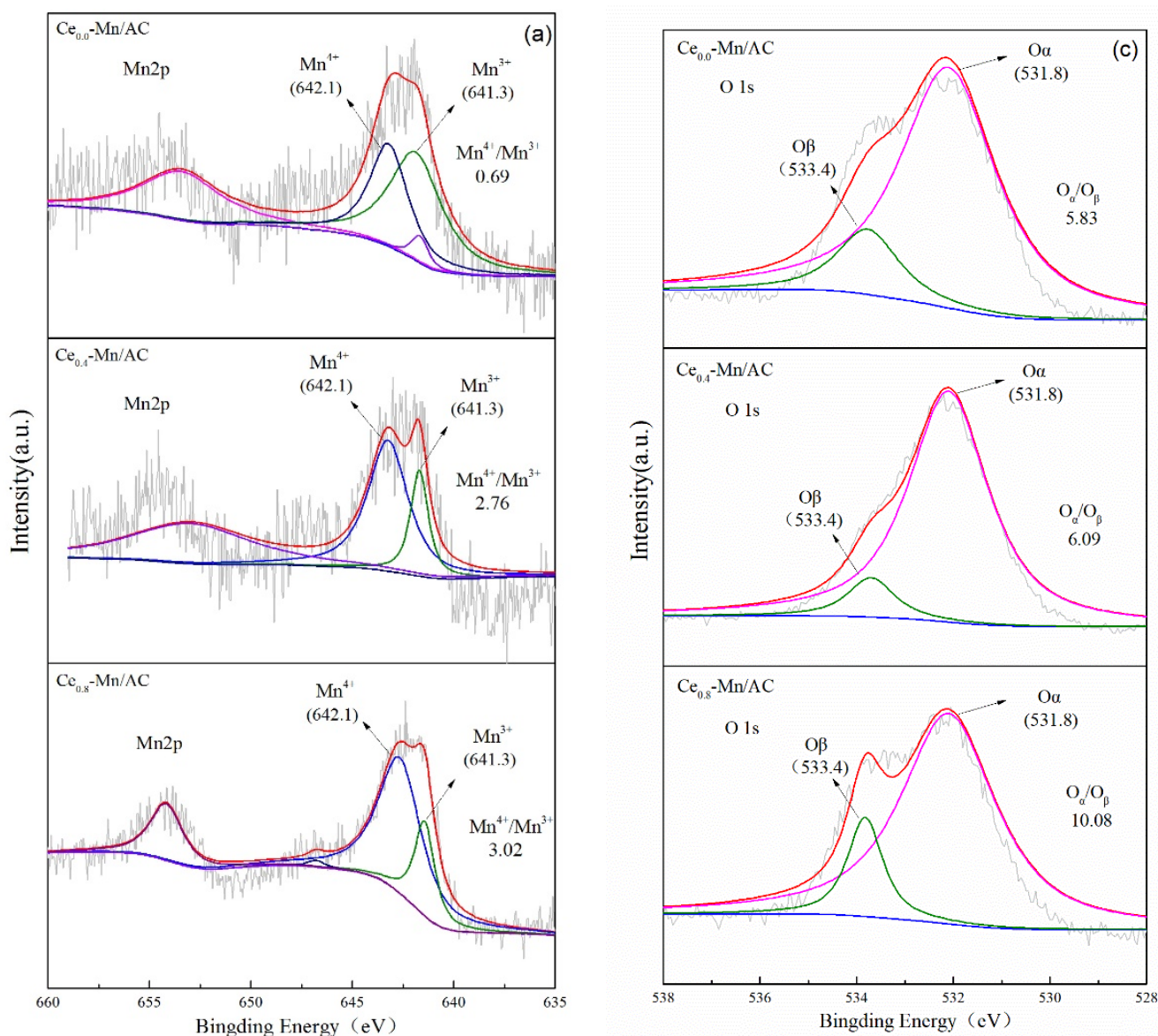
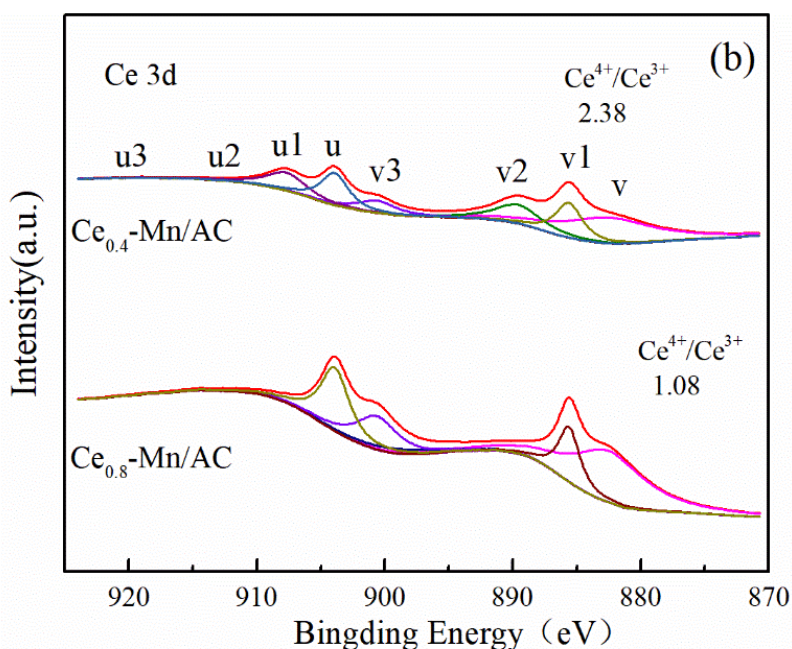


Figure 4. Cont.



**Figure 4.** XPS  $Mn_{2p}$  (a),  $Ce_{3d}$  (b) and  $O_{1s}$  (c) spectra on the catalysts.

SEM and TEM images of AC carrier,  $Ce_{0.4}\text{-Mn/AC}$ , and  $Ce_{0.8}\text{-Mn/AC}$  are shown in Figure 5. The original AC carrier presents a smooth surface (Figure 5a). After adding the active components to the AC carrier surface, the sample surface showed many highly dispersed raised structures. Samples of  $Ce_{0.8}\text{-Mn/AC}$  (Figure 5c) showed significantly more raised structures than  $Ce_{0.4}\text{-Mn/AC}$  (Figure 5b). The EDS results (Figure 5e,f) show that the Mn and Ce content on the surface of  $Ce_{0.8}\text{-Mn/AC}$  samples reached 5.64% and 0.75%, respectively, obviously higher than those of the  $Ce_{0.4}\text{-Mn/AC}$  samples. TEM test results of  $Ce_{0.8}\text{-Mn/AC}$  samples are shown in Figure 5d,g. A large amount of particulate metal oxide with different sizes was found and was highly dispersed on the surface of the AC. That larger ones with a diameter of about 10 nm interlace to the small ones with a diameter of 2–3 nm. According to the EDS element mapping of Mn (Figure 5h) and Ce (Figure 5i), all catalyst surfaces showed a large amount of Mn and Ce particles, which were highly and uniformly dispersed. This indicates that adding Ce helps improve Mn dispersibility on the surface of catalyst carriers, and highly dispersed Mn and Ce particles can further provide more active sites for the subsequent catalysis and enhance the overall catalytic performance [61,62].

### 3.2. Catalytic Performance of Catalysts for Acetone

At the acetone concentration of  $238\text{ mg/m}^3$  and the acetone conversion in the catalysts at different temperatures are shown in Figure 6a. When the temperature was below  $175\text{ }^\circ\text{C}$ , the acetone conversion of some samples was beneath zero, which is attributed to the adsorbed acetone in the porous structure at low temperatures released with the temperature increase, thus leading the outlet concentrations of acetone to be higher than the inlet concentrations. Taking the corresponding temperature at the acetone conversion of 50% ( $T_{50}$ ) and that at the acetone conversion of 90% ( $T_{90}$ ) as the criteria for catalyst activity, the catalyst activity of these samples is in the proper order of  $Ce_{0.8}\text{-Mn/AC}$ ,  $Ce_{0.4}\text{-Mn/AC}$ ,  $Ce_{0.6}\text{-Mn/AC}$ ,  $Ce_{0.2}\text{-Mn/AC}$ ,  $Ce_{1.0}\text{-Mn/AC}$ , and  $Ce_{0.0}\text{-Mn/AC}$ .  $Ce_{0.8}\text{-Mn/AC}$  showed the best acetone catalytic activity, and  $T_{50}$  and  $T_{90}$  were  $175$  and  $245\text{ }^\circ\text{C}$ , respectively. This is related to the highest dispersity of Mn and Ce particles on  $Ce_{0.8}\text{-Mn/AC}$  surfaces. Comparison with the acetone conversion of a similar types of catalysts reported by Lin and Liang-Yi [63] and Rezlescu [28] indicates that the  $Ce_{0.8}\text{-Mn/AC}$  prepared in this study exhibits excellent catalytic activity for acetone. Figure 6b shows the acetone degradation rate of  $Ce_{0.8}\text{-Mn/AC}$  over time under different catalyzing temperatures. At room temperature

(25 °C), the acetone conversion was first maintained at 100%. After 900 min, it declined gradually over time and finally maintained at a low level. This is mainly due to the acetone adsorption at a low temperature. As the temperature increases, the breakthrough time and amount of adsorption of acetone decrease because the acetone adsorption in carrier is an exothermic process [64]. At the same time, the catalytic activity of Ce<sub>0.8</sub>-Mn/AC for acetone increases. When the temperature exceeds 250 °C, the acetone conversion of Ce<sub>0.8</sub>-Mn/AC surpasses 90%, and at 280 °C, the acetone conversion is nearly 100%. At 250 °C, the conversion of Ce<sub>0.8</sub>-Mn/AC for acetone over time at different oxygen contents is shown in Figure 6c. As the oxygen content decreased, the acetone conversion was reduced as well. Lower oxygen content in the waste gas leads to fewer lattice oxygen and adsorption oxygen around Mn<sup>4+</sup> and Ce<sup>3+</sup> [65], and thus decreases the oxygen transfer rate in acetone degradation.

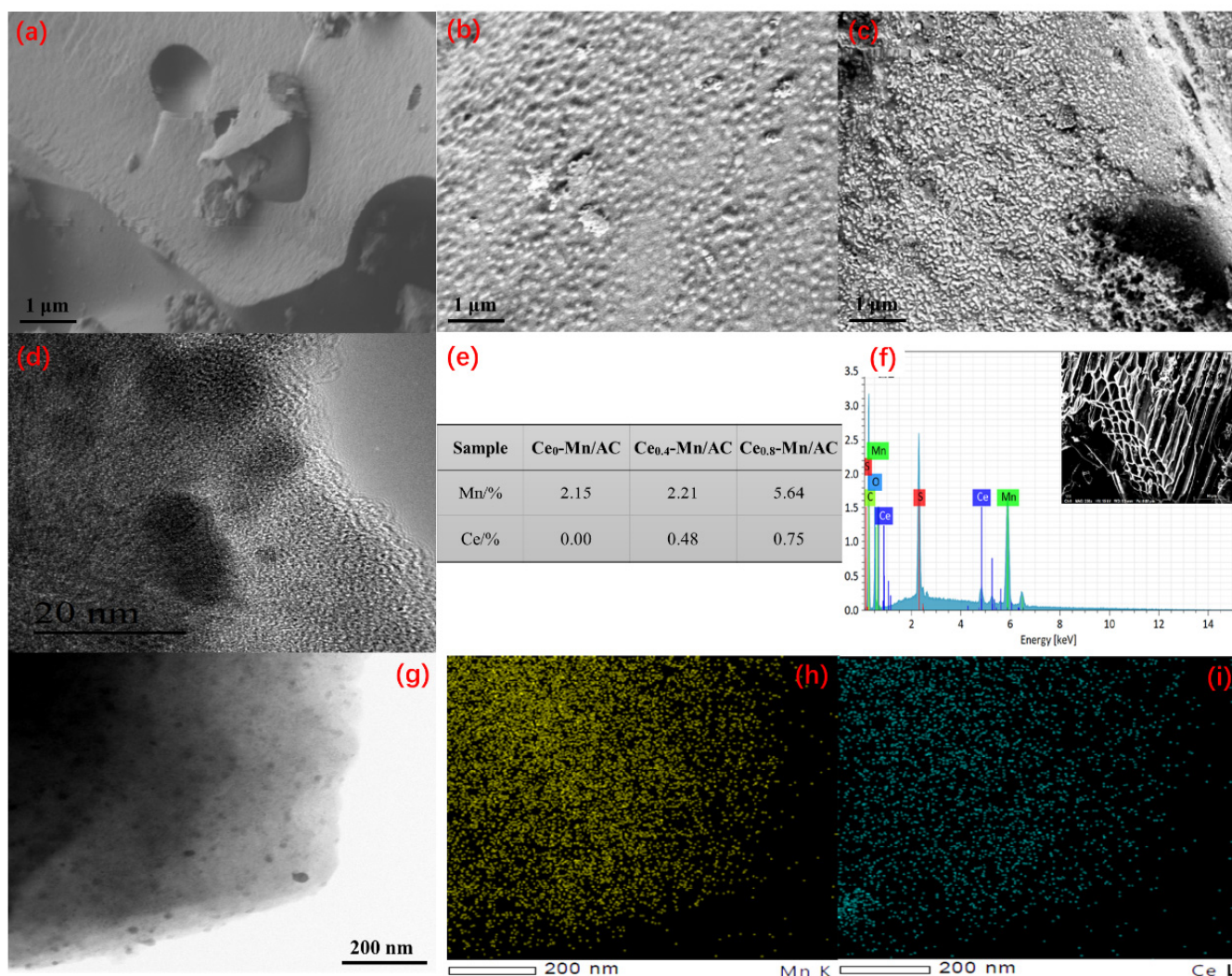


**Figure 5.** Scanning electron microscope (SEM) images of AC (a); Ce<sub>0.4</sub>-Mn/AC (b); Ce<sub>0.8</sub>-Mn/AC (c); transmission electron microscope (TEM) images of Ce<sub>0.8</sub>-Mn/AC (d,g); elemental contents of different catalysts (e); EDS spectra of Ce<sub>0.8</sub>-Mn/AC (f); EDS elemental mapping of Mn (h) and Ce (i) on the Ce<sub>0.8</sub>-Mn/AC.

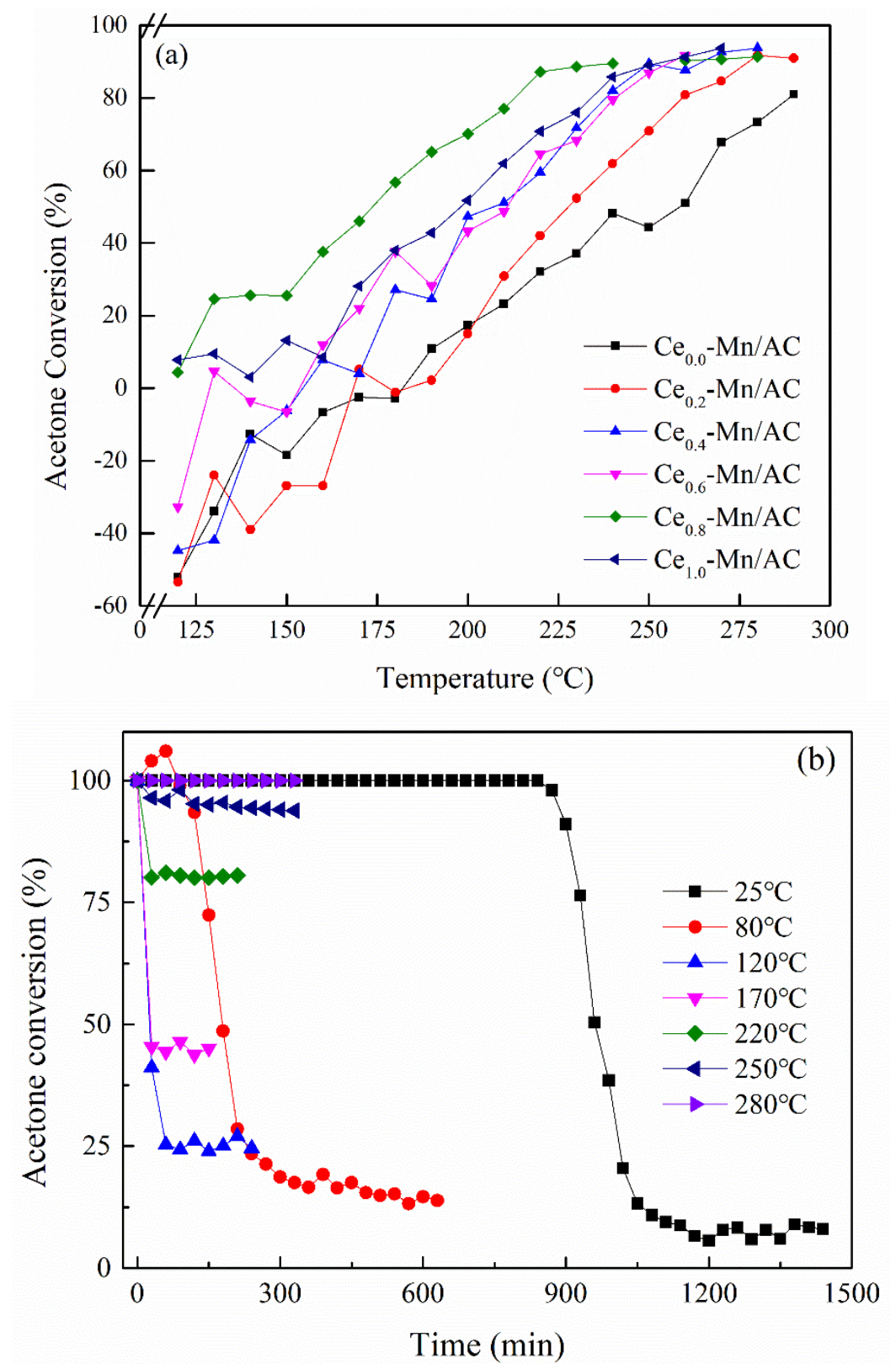
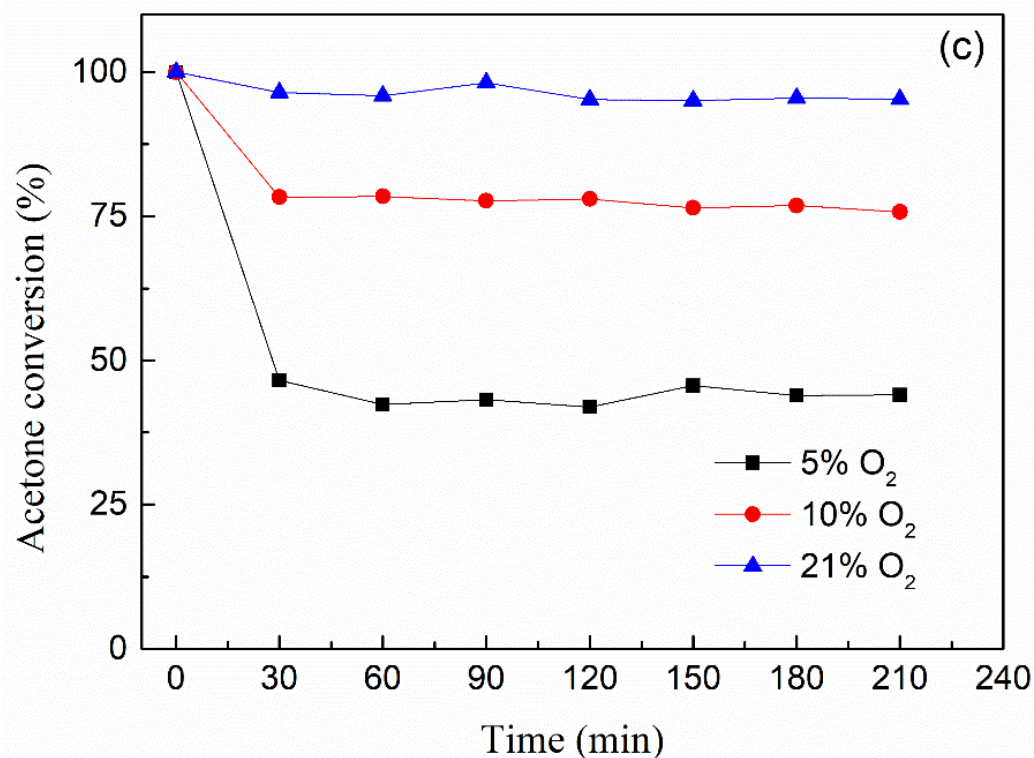


Figure 6. Cont.



**Figure 6.** The acetone conversion of the catalysts for acetone (a); effects of reaction temperature on the removal efficiency of acetone over Ce<sub>0.8</sub>-Mn/AC as a function of time (reaction conditions: acetone concentration = 238 mg/m<sup>3</sup>, oxygen content = 21%) (b); effects of oxygen content on the removal efficiency of acetone over Ce<sub>0.8</sub>-Mn/AC as a function of time (reaction conditions: acetone concentration = 238 mg/m<sup>3</sup>, reaction temperature = 250 °C) (c).

### 3.3. Mechanism of Catalytic Oxidation of the Ce<sub>0.8</sub>-Mn/AC

In recent years, researchers have delved into the catalytic oxidation mechanism of VOCs [66]. Active component particles coat the carrier surface as support, and VOC reactants are adsorbed onto the material surface. Adsorbed VOCs first react with lattice oxygen or adsorption oxygen on the surface of the catalyst carrier to form active intermediates. Then, the intermediaries desorb from the catalyst surfaces and react with each other to form inorganic compounds. Meanwhile, active sites losing lattice oxygen or adsorption oxygen can capture gaseous oxygen in the air to form lattice oxygen and adsorption oxygen again, and thereby regenerate the catalyst.

The reaction mechanism is shown in Figure 7. Highly dispersed CeO<sub>2</sub> on the catalyst surface provides large amounts of oxygen vacancies in the catalytic process. Ce atoms can connect with Mn and O and form the Mn-O-Ce bridge, and further reinforce Mn-O<sub>2</sub> binding. The bridge serves as a channel for the electron transfer between manganese and cerium cations [45,67]. During the thermal decomposition of CeO<sub>2</sub> into Ce<sub>2</sub>O<sub>3</sub> (Step1) [61], a large amount of adsorption oxygen is released, and thus it accelerates the conversion of Mn<sup>3+</sup> into Mn<sup>4+</sup> (Step4) [45,67]. In the meantime, it ensures timely oxygen atom supply to the surface when most of the lattice oxygen on the Mn<sup>3+</sup>/Mn<sup>4+</sup> surface is consumed [60]. Mn<sup>3+</sup> and Mn<sup>4+</sup> exhibit high oxidizing ability, and can release active oxygen (O\*) when reacting with acetone (Step2). Active oxygens react with acetone to form final degradation products (Step3) [66]. In addition, oxygen atoms in the air promptly make up the oxygen vacancies formed after reacting on the catalyst surface, and finish catalyst regeneration (Step5) [31,61,68]. The study results indicate that cerium oxide and manganese oxide are synergistic in the catalytic degradation of acetone. Adding cerium to manganese-based catalysts can increase the oxygen migration rate and lattice oxygen reduction rate.

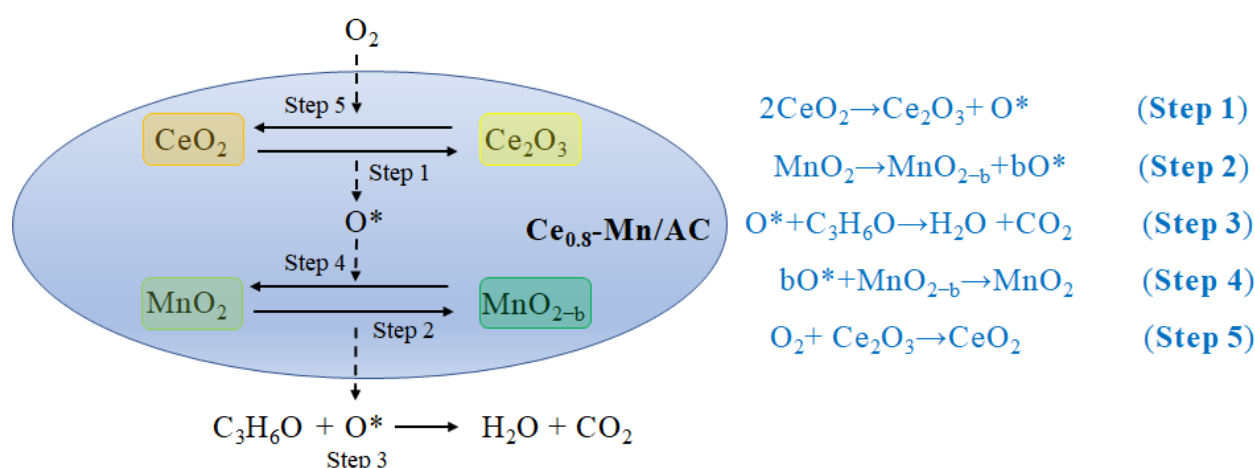


**Figure 7.** Schematic of catalysts of the acetone on Ce<sub>0.8</sub>-Mn/AC.

#### 4. Conclusions

With a porous carbon material prepared from citric acid residue as the carrier, the catalysts of different Ce-Mn ratios were prepared using the IWI method. When the molar ratio of Ce/Mn was 0.8, a large amount of Mn and Ce particles were highly and evenly distributed on the prepared catalyst Ce<sub>0.8</sub>-Mn/AC surfaces. The Mn and Ce contents on the Ce<sub>0.8</sub>-Mn/AC surface reached 5.64% and 0.75%, respectively. At the acetone concentration of 238 mg/m<sup>3</sup>, the catalytic activity of Ce<sub>0.8</sub>-Mn/AC for acetone was the best, and T<sub>50</sub> and T<sub>90</sub> values were 175 and 245 °C, respectively. During the degradation process, adding cerium to manganese-based catalysts improves the oxygen migration rate and the lattice oxygen reduction rate. The synergistic action of Ce and Mn improves the catalytic performance in acetone degradation at low temperatures. The research results provide new ideas for developing carbon-based catalysts for the efficient degradation of acetone.

**Author Contributions:** T.L.: Methodology, Writing—original draft; Z.W.: Resources; Y.S.: Resources; X.Y.: Data curation, Supervision. All authors have read and agreed to the published version of the manuscript.

**Funding:** This work was supported by the Beijing Natural Science Foundation (No. 8214055), the National Natural Science Foundation of China (No. 52100116), and the General Project of Beijing Educational Committee (KM202010011002).

**Conflicts of Interest:** The authors declare no conflict of interest.

#### References

- Cleaner Production Center of Ministry of Environmental Protection; China Fermentation Industry Association Research. *Report on Cleaner Production of Citric Acid Industry in China*; China Environmental Science Press: Beijing, China, 2013; ISBN 9787511114488.
- Yao, X.; Wang, K.; Zhang, S.; Liang, S.; Li, K.; Wang, C.; Zhang, T.; Li, H.; Wang, J.; Dong, L.; et al. Degradation of the mixture of ethyl formate, propionic aldehyde, and acetone by *Aeromonas salmonicida*: A novel microorganism screened from biomass generated in the citric acid fermentation industry. *Chemosphere* **2020**, *258*, 127320. [[CrossRef](#)] [[PubMed](#)]
- Yao, X.; Liu, Y.; Li, T.; Zhang, T.; Li, H.; Wang, W.; Shen, X.; Qian, F.; Yao, Z. Adsorption behavior of multicomponent volatile organic compounds on a citric acid residue waste-based activated carbon: Experiment and molecular simulation. *J. Hazard. Mater.* **2020**, *392*, 122323. [[CrossRef](#)] [[PubMed](#)]
- Chattopadhyay, A.; Chatterjee, P.; Chakraborty, T. Photo-oxidation of acetone to formic acid in synthetic air and its atmospheric implication. *J. Phys. Chem. A* **2015**, *119*, 8146–8155. [[CrossRef](#)] [[PubMed](#)]
- Ge, S.; Xu, Y.; Jia, L. Effects of inorganic seeds on secondary organic aerosol formation from photochemical oxidation of acetone in a chamber. *Atmos. Environ.* **2017**, *170*, 205–215. [[CrossRef](#)]
- Zhang, C.; He, H. A comparative study of TiO<sub>2</sub> supported noble metal catalysts for the oxidation of formaldehyde at room temperature. *Catal. Today* **2007**, *126*, 345–350. [[CrossRef](#)]
- Montecchio, F.; Babler, M.U.; Engvall, K. Development of an irradiation and kinetic model for UV processes in volatile organic compounds abatement applications. *Chem. Eng. J.* **2018**, *348*, 569–582. [[CrossRef](#)]
- Leoni, B.; Bettinetti, R.; Galassi, S. Sub-lethal effects of acetone on *Daphnia magna*. *Ecotoxicology* **2008**, *17*, 199–205. [[CrossRef](#)]

9. Xie, R.; Ji, J.; Huang, H.; Lei, D.; Fang, R.; Shu, Y.; Zhan, Y.; Guo, K.; Leung, D. Heterogeneous activation of peroxymonosulfate over monodispersed  $\text{Co}_3\text{O}_4$ /activated carbon for efficient degradation of gaseous toluene. *Chem. Eng. J.* **2018**, *341*, 383–391. [[CrossRef](#)]
10. Fu, D.; Feng, X.; Zhang, P. Absorption performance of ( $\text{CO}_2 + \text{N}_2$ ) gas mixtures in amino acid ionic liquids promoted N-methyldiethanolamine aqueous solutions. *J. Chem. Thermodyn.* **2017**, *113*, 250–256. [[CrossRef](#)]
11. Wang, Y.; Zhang, X.; Shen, B.; Smith, R.; Guo, H. Role of impurity components and pollutant removal processes in catalytic oxidation of o-xylene from simulated coal-fired flue gas. *Sci. Total Environ.* **2021**, *764*, 142805. [[CrossRef](#)] [[PubMed](#)]
12. Pan, K.; Pan, G.; Chong, S.; Chang, M. Removal of VOCs from gas streams with double perovskite-type catalysts. *J. Environ. Sci.* **2018**, *69*, 205–216. [[CrossRef](#)] [[PubMed](#)]
13. Lee, J.E.; Ok, Y.S.; Tsang, D.C.W.; Song, J.; Jung, S.C.; Park, Y.K. Recent advances in volatile organic compounds abatement by catalysis and catalytic hybrid processes: A critical review. *Sci. Total Environ.* **2020**, *719*, 137405. [[CrossRef](#)]
14. Li, Y.; Li, W.; Yuan, C.; Hung, C.; Shen, H. Photoelectrocatalytic degradation of gaseous acetone using electrical glassfiber filter coated with nano-sized  $\text{TiO}_2$  photoelectrocatalyst. *J. Taiwan Inst. Chem. Eng.* **2017**, *77*, 187–195. [[CrossRef](#)]
15. Banu, I.; Manta, C.M.; Bercaru, G.; Bozga, G. Combustion kinetics of cyclooctane and its binary mixture with o-xylene over a Pt/ $\gamma$ -alumina catalyst. *Chem. Eng. Res. Des.* **2015**, *102*, 399–406. [[CrossRef](#)]
16. Santos, V.P.; Pereira, M.F.R.; Orfao, J.J.M.; Figueiredo, J.L. The role of lattice oxygen on the activity of manganese oxides towards the oxidation of volatile organic compounds. *Appl. Catal. B* **2010**, *99*, 353–363. [[CrossRef](#)]
17. Piumetti, M.; Fino, D.; Russo, N. Mesoporous manganese oxides prepared by solution combustion synthesis as catalysts for the total oxidation of VOCs. *Appl. Catal. B* **2015**, *163*, 277–287. [[CrossRef](#)]
18. Ghavami, M.; Soltan, J. Kinetics and mechanism of catalytic ozonation of acetone in air over  $\text{MnO}_x/\text{Al}_2\text{O}_3$  catalyst. *React. Kinet. Mech. Catal.* **2021**, *133*, 953–970. [[CrossRef](#)]
19. Lin, H.; Liu, Y.; Deng, J.; Zhang, K.; Zhang, X.; Xie, S.; Zhao, X.; Yang, J.; Han, Z.; Dai, H. Au-Pd/mesoporous  $\text{Fe}_2\text{O}_3$ : Highly active photocatalysts for the visible-light-driven degradation of acetone. *J. Environ. Sci.* **2018**, *70*, 74–86. [[CrossRef](#)] [[PubMed](#)]
20. Inoue, K.; Somekawa, S. Treatment of volatile organic compounds with a Pt/ $\text{Co}_3\text{O}_4$ - $\text{CeO}_2$  catalyst. *Chem. Eng. Technol.* **2019**, *42*, 257–260. [[CrossRef](#)]
21. Xia, Y.; Xia, L.; Liu, Y.; Yang, T.; Deng, J.; Dai, H. Concurrent catalytic removal of typical volatile organic compound mixtures over Au-Pd/ $\alpha$ - $\text{MnO}_2$  nanotubes. *J. Environ. Sci.* **2018**, *64*, 276–288. [[CrossRef](#)] [[PubMed](#)]
22. Busca, G.; Berardinelli, S.; Resini, C.; Arrighi, L. Technologies for the removal of phenol from fluid streams: A short review of recent developments. *J. Hazard. Mater.* **2008**, *160*, 265–288. [[CrossRef](#)] [[PubMed](#)]
23. Changsuphan, A.; Oanh, N.T.K. Catalytic oxidation of volatile organic compounds by 13X zeolite coated with nZnO in presence of UV and ozone at high bed temperature. *Water Air Soil Pollut.* **2018**, *229*, 201. [[CrossRef](#)]
24. He, C.; Jiang, Z.; Ma, M.; Zhang, X.; Douthwaite, M.; Shi, J.; Hao, Z. Understanding the promotional effect of  $\text{Mn}_2\text{O}_3$  on micro-/mesoporous hybrid silica nanocubic-supported Pt catalysts for the low-temperature destruction of methyl ethyl ketone: An experimental and theoretical study. *ACS Catal.* **2018**, *8*, 4213–4229. [[CrossRef](#)]
25. Chen, Z.; Li, J.; Yang, P.; Cheng, Z.; Li, J.; Zuo, S. Ce-modified mesoporous  $\gamma$ - $\text{Al}_2\text{O}_3$  supported Pd-Pt nanoparticle catalysts and their structure-function relationship in complete benzene oxidation. *Chem. Eng. J.* **2019**, *356*, 255–261. [[CrossRef](#)]
26. Liu, P.; He, H.; Wei, G.; Liang, X.; Qi, F.; Tan, F.; Tan, W.; Zhu, J.; Zhu, R. Effect of Mn substitution on the promoted formaldehyde oxidation over spinel ferrite: Catalyst characterization, performance and reaction mechanism. *Appl. Catal. B* **2016**, *182*, 476–484. [[CrossRef](#)]
27. Hu, C. Catalytic combustion kinetics of acetone and toluene over  $\text{Cu}_{0.13}\text{Ce}_{0.87}\text{O}_y$  catalyst. *Chem. Eng. J.* **2011**, *168*, 1185–1192. [[CrossRef](#)]
28. Rezlescu, N.; Rezlescu, E.; Popa, P.D.; Doroftei, C.L.; Ignat, M. Some nanograined ferrites and perovskites for catalytic combustion of acetone at low temperature. *Ceram. Int.* **2015**, *41*, 4430–4437. [[CrossRef](#)]
29. Li, G.; Hu, R.C.; Hao, Y.H.; Yang, T.L.; Li, L.L.; Luo, Z.H.; Xie, Y.J.; Zhao, N.; Liu, C.; Sun, C.; et al.  $\text{CO}_2$  and air pollutant emissions from bio-coal briquettes. *Environ. Technol. Innov.* **2023**, *29*, 102975. [[CrossRef](#)]
30. Guo, S.J.; Sun, S.H. FePt nanoparticles assembled on graphene as enhanced catalyst for oxygen reduction reaction. *J. Am. Chem. Soc.* **2012**, *134*, 2492–2495. [[CrossRef](#)] [[PubMed](#)]
31. Singh, R.; Tripathi, K.; Pant, K.K. Investigating the role of oxygen vacancies and basic site density in tuning methanol selectivity over Cu/ $\text{CeO}_2$  catalyst during  $\text{CO}_2$  hydrogenation. *Fuel* **2021**, *303*, 121289. [[CrossRef](#)]
32. Li, G.; Hu, R.; Wang, N.; Yang, T.; Xu, F.; Li, J.; Wu, J.; Huang, Z.; Pan, M.; Lyu, T. Cultivation of microalgae in adjusted wastewater to enhance biofuel production and reduce environmental impact: Pyrolysis performances and life cycle assessment. *J. Clean. Prod.* **2022**, *355*, 131768. [[CrossRef](#)]
33. Li, G.; Yang, T.L.; Xiao, W.B.; Wu, J.H.; Xu, F.Z.; Li, L.L.; Gao, F.; Huang, Z.G. Sustainable environmental assessment of waste-to-energy practices: Co-pyrolysis of food waste and discarded meal boxes. *Foods* **2022**, *11*, 3840. [[CrossRef](#)] [[PubMed](#)]
34. Qu, J.; Zhou, S.; Wang, H.; Cao, Z.; Liu, H. The application of an activated carbon supported Cu-Ce/AC oxide anode on the electrocatalytic degradation of phenol. *Int. J. Electrochem. Sci.* **2017**, *12*, 9640–9651. [[CrossRef](#)]
35. Qin, H.; Xiao, R.; Chen, J. Catalytic wet peroxide oxidation of benzoic acid over Fe/AC catalysts: Effect of nitrogen and sulfur co-doped activated carbon. *Sci. Total Environ.* **2018**, *626*, 1414–1420. [[CrossRef](#)] [[PubMed](#)]

36. Zhang, X.; Dong, Y.; Cui, L.; An, D.; Feng, Y. Removal of elemental mercury from coal pyrolysis gas using Fe–Ce oxides supported on lignite semi-coke modified by the hydrothermal impregnation method. *Energy Fuels* **2018**, *32*, 12861–12870. [[CrossRef](#)]
37. Chen, Z.; Liu, L.; Qu, H.; Zhong, Q.; Liu, Z. The effect of CeO<sub>2</sub> dispersity and active oxygen species on the SCR reaction over Fe-ZSM-5@Ce/meso-SiO<sub>2</sub>. *Catal. Lett.* **2019**, *150*, 514–523. [[CrossRef](#)]
38. Guo, Y.; Sun, Y.; Yang, D.; Dai, J.; Liu, Z.; Chen, Y.; Huang, J.; Li, Q. Biogenic Pt/CaCO<sub>3</sub> nanocomposite as a robust catalyst toward benzene oxidation. *ACS Appl. Mater. Interfaces* **2020**, *12*, 2469–2480. [[CrossRef](#)]
39. Jafari, A.J.; Kalantary, R.R.; Esrafilia, A.; Arfaenia, H. Synthesis of silica-functionalized graphene oxide/ZnO coated on fiberglass and its application in photocatalytic removal of gaseous benzene. *Process Saf. Environ. Prot.* **2018**, *116*, 377–387. [[CrossRef](#)]
40. Dong, Z. *Study on Denitrification Performance and Synergistic Catalytic Mechanism of Nano-Mn-Ce Oxide*; Chongqing University: Chongqing, China, 2016.
41. Yorgun, S.; Yıldız, D. Preparation and characterization of activated carbons from Paulownia wood by chemical activation with H<sub>3</sub>PO<sub>4</sub>. *J. Taiwan Inst. Chem. Eng.* **2015**, *53*, 122–131. [[CrossRef](#)]
42. Bianchi, C.L.; Gotti, E.; Toscano, L.; Ragaini, V. Preparation of Pd/C catalysts via ultrasound: A study of the metal distribution. *Ultrason. Sonochem.* **1997**, *4*, 317–320. [[CrossRef](#)] [[PubMed](#)]
43. Chen, W.; Ni, J. Different effects of surface heterogeneous atoms of porous and non-porous carbonaceous materials on adsorption of 1,1,2,2-tetrachloroethane in aqueous environment. *Chemosphere* **2017**, *175*, 323–331. [[CrossRef](#)] [[PubMed](#)]
44. Li, G.; Hao, Y.; Yang, T.; Xiao, W.; Pan, M.; Huo, S.; Lyu, T. Enhancing bioenergy production from the raw and defatted microalgal biomass using wastewater as the cultivation medium. *Bioengineering* **2022**, *9*, 637. [[CrossRef](#)] [[PubMed](#)]
45. Jiang, L.; Liu, Q.; Zhao, Q.; Ren, S.; Kong, M.; Yao, L.; Meng, F. Promotional effect of Ce on the SCR of NO with NH<sub>3</sub> at low temperature over MnO<sub>x</sub> supported by nitric acid-modified activated carbon. *Res. Chem. Intermed* **2017**, *44*, 1729–1744. [[CrossRef](#)]
46. Li, Z.; Guo, X.; Tao, F.; Zhou, R. New insights into the effect of morphology on catalytic properties of MnO<sub>x</sub>–CeO<sub>2</sub> mixed oxides for chlorobenzene degradation. *RSC Adv.* **2018**, *8*, 25283–25291. [[CrossRef](#)] [[PubMed](#)]
47. Lin, J.; Guo, Y.; Chen, X.; Li, C.; Lu, S.; Liew, K. CO Oxidation over nanostructured ceria supported bimetallic Cu–Mn oxides catalysts: Effect of Cu/Mn ratio and calcination temperature. *Catal. Lett.* **2017**, *148*, 181–193. [[CrossRef](#)]
48. Jampaiah, D.; Tur, K.M.; Venkataswamy, P.; Ippolito, S.J.; Sabri, Y.M.; Tardio, J.; Bhargava, S.K.; Reddy, B.M. Catalytic oxidation and adsorption of elemental mercury over nanostructured CeO<sub>2</sub>–MnO<sub>x</sub> catalyst. *RSC Adv.* **2015**, *5*, 30331–30341. [[CrossRef](#)]
49. Zhao, Q.; Liu, Q.; Han, J.; Lu, S.; Su, Y.; Song, C.; Ji, N.; Lu, X.; Ma, D.; Cheung, O. The effect of cerium incorporation on the catalytic performance of cobalt and manganese containing layer double oxides for acetone oxidation. *J. Chem. Technol. Biotechnol.* **2018**, *94*, 3753–3762. [[CrossRef](#)]
50. Li, G.; Hao, Y.; Yang, T.; Wu, J.; Xu, F.; Li, L.; Wang, B.; Li, M.; Zhao, N.; Wang, N.; et al. Air pollutant emissions from sludge-bituminous briquettes as a potential household energy source. *Case Stud. Therm. Eng.* **2022**, *37*, 102251. [[CrossRef](#)]
51. He, J.; Reddy, G.K.; Thiel, S.W.; Smirniotis, P.G.; Pinto, N.G. Ceria-modified manganese oxide/titania materials for removal of elemental and oxidized mercury from flue gas. *J. Phys. Chem. C* **2011**, *115*, 24300–24309. [[CrossRef](#)]
52. Liu, Z.; Zhang, S.; Li, J.; Zhu, J.; Ma, L. Novel V<sub>2</sub>O<sub>5</sub>–CeO<sub>2</sub>/TiO<sub>2</sub> catalyst with low vanadium loading for the selective catalytic reduction of NO<sub>x</sub> by NH<sub>3</sub>. *Appl. Catal. B* **2014**, *158*, 11–19. [[CrossRef](#)]
53. Liu, Y.; Hu, C.; Bian, L. Highly dispersed Pd species supported on CeO<sub>2</sub> catalyst for lean methane combustion: The effect of the occurrence state of surface Pd species on the catalytic activity. *Catalysts* **2021**, *11*, 772. [[CrossRef](#)]
54. Wang, Z.; Lin, F.; Jiang, S.; Qiu, K.; Kuang, M.; Whiddon, R.; Cen, K. Ceria substrate–oxide composites as catalyst for highly efficient catalytic oxidation of NO by O<sub>2</sub>. *Fuel* **2016**, *166*, 352–360. [[CrossRef](#)]
55. Feng, Z. *Preparation of Cerium Oxide Based Catalysts by Flame Combustion Method and CO Oxidation Performance*; University of Chinese Academy of Sciences: Beijing, China, 2019.
56. He, C.; Yu, Y.; Yue, L.; Qiao, N.; Li, J.; Shen, Q.; Yu, W.; Chen, J.; Hao, Z. Low-temperature removal of toluene and propanal over highly active mesoporous CuCeO<sub>x</sub> catalysts synthesized via a simple self-precipitation protocol. *Appl. Catal. B* **2014**, *147*, 156–166. [[CrossRef](#)]
57. Huang, Z.; Zhang, J.; Pan, M.; Hao, Y.; Hu, R.; Xiao, W.; Li, G.; Lyu, T. Valorisation of microalgae residues after lipid extraction: Pyrolysis characteristics for biofuel production. *Biochem. Eng. J.* **2022**, *179*, 108330. [[CrossRef](#)]
58. Lv, K.; Xiang, Q.; Yu, J. Effect of calcination temperature on morphology and photocatalytic activity of anatase TiO<sub>2</sub> nanosheets with exposed {001} facets. *Appl. Catal. B* **2011**, *104*, 275–281. [[CrossRef](#)]
59. Wang, X.; Zhao, W.; Zhang, T.; Zhang, Y.; Jiang, L.; Yin, S. Facile fabrication of shape-controlled Co<sub>x</sub>Mn<sub>y</sub>O<sub>beta</sub> nanocatalysts for benzene oxidation at low temperatures. *Chem. Comm.* **2018**, *54*, 2154–2157. [[CrossRef](#)]
60. Zhu, L.; Yu, J.; Wang, X. Oxidation treatment of diesel soot particulate on Ce<sub>x</sub>Zr<sub>1-x</sub>O<sub>2</sub>. *J. Hazard. Mater.* **2007**, *140*, 205–210. [[CrossRef](#)]
61. Xie, Y.; Li, C.; Zhao, L.; Zhang, J.; Zeng, G.; Zhang, X.; Zhang, W.; Tao, S. Experimental study on Hg<sup>0</sup> removal from flue gas over columnar MnO<sub>x</sub>–CeO<sub>2</sub>/activated coke. *Appl. Surf. Sci.* **2015**, *333*, 59–67. [[CrossRef](#)]
62. Zhang, H.; Zhu, Y.; Wang, S.; Zhao, M.; Gong, M.; Chen, Y. Activity and thermal stability of Pt/Ce<sub>0.64</sub>Mn<sub>0.16</sub>R<sub>0.2</sub>O<sub>x</sub> (R=Al, Zr, La, or Y) for soot and NO oxidation. *Fuel Process. Technol.* **2015**, *137*, 38–47. [[CrossRef](#)]
63. Lin, L.; Wang, C.; Bai, H. A comparative investigation on the low-temperature catalytic oxidation of acetone over porous aluminosilicate-supported cerium oxides. *Chem. Eng. J.* **2015**, *264*, 835–844. [[CrossRef](#)]

64. Kam, S.K.; Kang, K.H.; Lee, M.G. Adsorption characteristics of acetone, benzene, and methylmercaptan in the fixed bed reactor packed with activated carbon prepared from waste citrus peel. *Appl. Chem. Eng.* **2018**, *29*, 28–36. [[CrossRef](#)]
65. Chai, H.; Zhang, Z.; Zhou, Y.; Zhu, L.; Lv, H.; Wang, N. Roles of intrinsic Mn(3+) sites and lattice oxygen in mechanochemical debromination and mineralization of decabromodiphenyl ether with manganese dioxide. *Chemosphere* **2018**, *207*, 41–49. [[CrossRef](#)]
66. He, C.; Cheng, J.; Zhang, X.; Douthwaite, M.; Pattison, S.; Hao, Z. Recent advances in the catalytic oxidation of volatile organic compounds: A review based on pollutant sorts and sources. *Chem. Rev.* **2019**, *119*, 4471–4568. [[CrossRef](#)] [[PubMed](#)]
67. Feng, X.; Liu, H.; He, C.; Shen, Z.; Wang, T. Synergistic effect and mechanism of non-thermal plasma catalysis system in volatile organic compounds removal: A review. *Catal. Sci. Technol.* **2018**, *8*, 936–954. [[CrossRef](#)]
68. Almukhlifi, H.A.; Burns, R.C. The complete oxidation of isobutane over CeO<sub>2</sub> and Au/CeO<sub>2</sub>, and the composite catalysts MO<sub>x</sub>/CeO<sub>2</sub> and Au/MO<sub>x</sub>/CeO<sub>2</sub> (Mn<sup>+</sup> = Mn, Fe, Co and Ni): The effects of gold nanoparticles obtained from *n*-hexanethiolate-stabilized gold nanoparticles. *J. Mol. Catal. A Chem.* **2016**, *415*, 131–143. [[CrossRef](#)]